



Investigations into the residual multipath errors of choke-ring geodetic antennas on GNSS carrier-phase measurements

Lawrence Lau¹

Received: 10 April 2024 / Accepted: 2 December 2024
© The Author(s) 2024

Abstract

For about three decades, the Global Navigation Satellite System (GNSS) has been used for high-precision positioning in scientific and engineering applications, such as deformation monitoring for seismicity and volcano eruption. Such high-precision positioning applications require millimeter-level positioning accuracy. There are many man-made and natural reflective surfaces near the GNSS receiving antennas. GNSS signals can be reflected and then arrive at the GNSS antenna. The multipath effect occurs when the direct signal is mixed with the reflected signal at the GNSS receiver. Choke-ring antennas are designed to mitigate the multipath effect of reflected signals from below the horizontal plane of the GNSS receiving antenna. Moreover, GNSS receiving antennas at network/permanent stations are usually installed on tall pillars or monuments to prevent multipath from “ground” reflected signals. However, part of the reflected signals can still arrive at the GNSS antenna center and cause multipath errors in GNSS measurements. How much can the multipath effect be on the real-time GNSS-measured displacements in studies on seismicity and volcano eruption? This work investigates the below-the-horizon multipath effect of choke-ring antennas on GNSS carrier-phase measurements. Here we show the differenced carrier-phase multipath errors of two commonly used GNSS antennas at the International GNSS Service (IGS) tracking stations can reach 8 mm, the maximum, with the mean and SD in a few millimeters at the 95% confidence level. The findings of this work should be applicable to other choke-ring antennas with similar architecture.

Keywords Carrier-phase multipath errors · Choke-ring geodetic antennas · GNSS high-precision positioning · GNSS high-accuracy positioning

Introduction

GNSS is the collective team of the US Global Positioning System (GPS), Russian Global'naya Navigatsionnaya Sputnikovaya Sistema (GLONASS), European Galileo, Chinese BeiDou Navigation Satellite System (BDS), and other regional augmentation systems. High-precision GNSS has been used for deformation/displacement monitoring in earthquake and volcano eruption studies since the 1990s. GPS was used to measure displacements from the 28 June 1992 Landers earthquake sequence (Blewitt et al. 1993). GPS was used to monitor the deformation of triggered seismicity (Hager et al. 2021). GNSS was used to detect

the displacements due to the Nyiragongo volcano eruption in May 2022 (Smittarello et al. 2022). There are other examples of using GNSS/GPS in deformation/displacement monitoring (Roman and Lundgren 2021; Farquharson and Amelung 2020; Piecuch et al. 2018). The use of carrier-phase measurements in high-precision GNSS positioning can achieve millimeters or better positioning accuracy when the observation time is long (more than four hours usually). Long observation time aims to average out the carrier-phase multipath errors in the position solution. However, the efficiency of this multipath error averaging approach depends on the site environment and the satellite geometry during the observation period. Nevertheless, a long observation time for a single-position solution is impossible for real-time deformation/displacement monitoring. Jet Propulsion Laboratory (JPL) introduced a design of a choke ring for geodetic antennas (Filippov et al. 1998; Tatarnikov et al. 2011) in the late 1990s. Choke-ring antennas are designed to mitigate the multipath effect. However, reflected signals above the

✉ Lawrence Lau
lsgi-lawrence.lau@polyu.edu.hk

¹ Department of Land Surveying and Geo-Informatics, The Hong Kong Polytechnic University, Hong Kong, China

horizontal plane of the antenna can still arrive at the antenna phase center and cause multipath errors in measurements. Moreover, the reflected signals below the horizontal plane of the antenna may cause multipath errors in measurements as well. IGS tracking stations are usually located in less reflective environments, and the choke-ring antennas are mounted on tall pillars/monuments. IGS station information website shows that their stations are affected by multipath; Root Mean Square (RMS) pseudorange multipath errors of L1 and L2 frequencies (i.e., MP1 and MP2, respectively) per GNSS system (not per satellite) are shown. It was suggested that multipath could be prevented when the distances from the antenna to any reflective surfaces (e.g., water and metal surfaces) are more than 200 m (ComNav 2024). However, this condition is impossible because the ground itself is a reflective surface. It was stated that anything we put near an antenna would affect the antenna signal response (Schupler and Clark 2001). Multipath is a natural enemy of GNSS! With the state-of-the-art multipath mitigating antenna and optimal site selection, we still have to tolerate multipath contaminating GNSS measurements. How much can the below-antenna multipath affect the high-precision carrier-phase measurements? What is the multipath mitigation efficiency of the state-of-the-art choke-ring antennas? In other words, how does multipath affect the positioning accuracy in static GNSS positioning applications such as in real-time deformation/displacement monitoring of earthquakes and volcano eruptions?



Fig. 1 Experimental setup for below-antenna multipath data collection. A steel panel was used to generate controlled and strong reflected signals at the rover antenna

Methods

To obtain the carrier-phase multipath errors (in measurements, not in tracking loops) resulting from the reflected signals below the horizontal plane of the choke-ring antennas, the following procedure was carried out:

- i) GNSS multipath data collection in a well-controlled site.
- ii) Determination of the orbit repeated periods of multipathing satellites.
- iii) Determination of the period of the controlled reflection.
- iv) GNSS carrier-phase multipath error retrieval.

The details of the above steps are described as follows.

GNSS multipath data collection

Usually, MP1 and MP2 are used to study the multipath effect in measurements. MP1 and MP2 were used to analyze the multipath mitigation performance of a rover receiver Trimble R8 model 2 with TRM60158.00 (internal) antenna and a reference-station receiver Trimble NetR5 with TRM55971.00 groundplane antenna (Tang et al. 2013). However, MP1 and MP2 only show the multipath effect on pseudorange measurements. Regarding high-precision positioning for geodetic applications, we want to know the impact of choke-ring antennas on carrier-phase measurements. Therefore, this work investigates the effect of below-antenna reflected signals and choke-ring antennas on carrier-phase measurements (i.e., carrier-phase multipath errors).

GNSS multipath data collection in a well-controlled environment was carried out on the roof of the DE Wing of the Hong Kong Polytechnic University. To create controlled below-antenna reflected signals, a 1.5 m (height) x 1.8 m (wide) steel panel was set about 1 m to the north of a station (named rover antenna or station), as shown in Fig. 1. The steel panel is made of 316 L stainless steel. 316 L steel is the most commonly used austenitic stainless steel in the automotive industry and man-made structures/buildings. Two widely used geodetic antennas in the IGS global tracking network are selected for the multipath mitigation test in this work. The geodetic antennas are the Leica AR20 and Trimble GNSS-Ti Choke Ring v2 with SCIS Dome; the brief specifications of the two antennas are shown in Table 1. On 20 Feb. 2024, 17 IGS stations installed the Leica AR20, and 99 stations installed the Trimble GNSS Choke Ring antennas (including GNSS-Ti Choke Ring and GNSS-Ti Choke Ring v2). A reference station was set about 6 m from the rover station to form a very short baseline for an unbiased multipath investigation. Except for multipath errors

Table 1 Brief specifications of the Leica AR20 and Trimble GNSS Ti-V2 Choke Ring antennas (obtained from the Leica GR30/GM30/GR50 user Manual and Trimble GNSS Ti-V2 Choke Ring antenna brochure)

	Leica AR20 GNSS Choke Ring antenna	Trimble GNSS Ti-V2 Choke Ring antenna
Voltage	3.3 V to 12 V DC	3.5 V to 20 V DC
Supply current (maximum)	100 mA	125 mA
LNA Gain (typical)	29 dBi	-
Antenna gain	-	50 dB \pm 2dB
Antenna calibration data	See the IGS ANTEX file	

Table 2 Brief antenna-related specifications of the Septentrio AsteRx-m3 pro+GNSS receiver (obtained from the Septentrio AsteRx-m3 pro+datasheet)

Antenna supply voltage	3–5.5 V DC
Maximum antenna current	150 mA
Antenna gain range	15–45 dB

and random noise, all other GNSS biases and errors are eliminated by differencing (i.e., double differencing (DD)) the observations between the reference and rover stations. Since the coordinates of the reference and rover stations are known by pre-survey, the “true” DD residuals contain the carrier-phase multipath errors and random noise. Three-level Wavelet Daubechies 4 (db4) was used as a low-pass filter for the “true” DD residuals to obtain the DD carrier-phase multipath errors (Lau 2017). A Septentrio AsteRx-m3 Pro+GNSS receiver was used at the rover station; the brief specifications related to the antenna are shown in Table 2. A Leica GR50 GNSS receiver and a Leica AR25 choke-ring antenna were used at the reference station. No multipath mitigation was turned on at the GNSS receivers; it is the

exact setting/requirement for IGS stations - Guideline number 2.2.19 (IGS 2015).

On the other hand, a lightweight Trimble R12 (non-choke-ring) antenna was set up at the rover station to show the repeated carrier-phase multipath errors in the presence of the steel panel in consecutive and discrete sidereal days (because of different ground track repeatability among GNSS). These strong and clear carrier-phase multipath errors in time series are used for the determination of repeated orbit time of satellites. Moreover, the lightweight Trimble R12 antenna was set up at the rover station with and without the nearby steel panel on consecutive sidereal days (i.e., 8–10 November 2022). The later setup shows the change of carrier-phase multipath errors due to the reflection on the nearby steel panel and reflection from the environment (mainly from the ground). The use of this data set for sidereal time shift determination is described in Sect. 2.2 while the use of this data set for showing the effect of the steel panel on carrier-phase multipath errors is described in Sect. 3.1.

Since the ground-track repeatability of GNSS systems are different, observations carried out for this investigation are shown in Table 3. Carrier-phase multipath errors of tracking satellites of a static antenna repeat when the satellite geometry repeats. For instance, GPS satellite geometry repeats every sidereal day, and so do the multipath errors at a static antenna in the same environment. All data sets were collected on sunny days.

Determination of the orbit repeated periods of multipathing satellites

GNSS satellites may have slight differences in orbital time periods. For example, the sidereal time shifts of two

Table 3 Information on antennas used and the dates of GNSS data collection

Date (DOY)	Antenna at Rover station	Remark
19 Sept 2022 (262)	Trimble R12 integrated antenna	To show the multipath effect at the rover station without a choke-ring antenna
20 Sept 2022 (263)	Trimble R12 integrated antenna	
21 Sept 2022 (264)	Trimble R12 integrated antenna	
22 Sept 2022 (265)	Trimble GNSS-Ti-V2	Repeated GPS satellite geometry
23 Sept 2022 (266)	Trimble GNSS-Ti-V2	
24 Sept 2022 (267)	Leica AR20	Repeated GPS satellite geometry
25 Sept 2022 (268)	Leica AR20	
29 Sept 2022 (272)	Trimble GNSS-Ti-V2	Repeated Galileo satellite geometry w.r.t. 22 Sept. 2022 Repeated BDS MEO satellite geometry w.r.t. 22 Sept. 2022 To show the multipath effect
2 Oct 2022 (275)	Trimble GNSS-Ti-V2	To show the multipath effect
3 Oct 2022 (276)	Trimble GNSS-Ti-V2	Repeated GPS satellite geometry w.r.t. 2 Oct. 2022 with an anti-reflection sheet below the antenna
8 Nov 2022 (312)	Trimble R12 integrated antenna	Repeated GPS/GNSS satellite geometry w.r.t. 19–21 Sept. 2022
9 Nov 2022 (313)	Trimble R12 integrated antenna	With the reflective steel panel nearby
10 Nov 2022 (314)	Trimble R12 integrated antenna	Repeated GPS satellite geometry w.r.t. 9 Nov. 2022 Without the reflective steel panel nearby

consecutive days of GPS satellites can be in the range of 235–250 s (Lau 2012). The repeat time of GPS constellation can be determined by cross-correlation of double differences, computation from the individual ephemeris, etc. (Lau 2012; Seeber et al. 1998; Agnew and Larson 2007). The repeat orbit periods of multipathing GNSS satellites are determined by cross-correlation of denoised DD time-series data of sidereal days in this work. Data collected with Trimble R12 (non-choke-ring antenna) at the rover station on 2022 DOYs 262, 263, 264, 312, and 313 are used to determine the repeat orbit periods of multipathing GNSS satellites; strong and clear multipath errors can have better cross-correlation results. It has been checked that no satellite manoeuvre or repositioning occurred in the observation period of this work. An example of this step is shown in Fig. 2, where the time series of repeated L1 multipath errors of GPS satellite PRN 25 on two consecutive sidereal days (2022 DOYs 312 and 313) are aligned.

Determination of the period of the controlled reflection

With the determined repeat orbit periods of multipathing satellites in the above step, the periods for reflection from the steel panel can be found by comparing the denoised carrier-phase residuals (i.e., multipath errors) of the aligned time series. An example of this step is shown in Fig. 3, a time series of repeated L1 multipath errors of GPS satellite PRN 25 on three consecutive sidereal days (2022 DOYs

313–314) in which the last day (DOY 314) has no reflective steel panel near the rover receiver. The amplitude of the carrier-phase multipath errors on DOY 314 is lower than those on DOYs 312 and 313 in the rectangular window in Fig. 3. Therefore, the period of the rectangular window can be identified as the period of having reflection from the steel panel for the multipathing satellite; all other “background” reflections (i.e., apart from the steel panel) of DOY 314 are very similar to those of DOY 312 and 313. The complete statistical results of the Trimble R12 DOYs 312–314 data sets are described in Sect. 3.1 and Tables 4 and 5.

To obtain more samples for this investigation without the need for repeated ground tracks in all the data sets, the ray-tracing method (Lau and Cross 2007) has also been used to identify the period of the carrier-phase multipath errors generated from the steel panel.

GNSS carrier-phase multipath error retrieval

No object/surface is above the horizontal planes of the reference and rover antennas within 15 m of the data collection site. Geodetic GNSS receivers can effectively mitigate far-field multipath (Fenton and Jones 2005). Multipath errors in the collected GNSS measurements mainly come from the reflective surfaces below the horizontal planes of the reference and rover antennas. As shown in Fig. 2, the DD carrier-phase multipath errors can reach 2 cm or more. It means that reflected signals may still arrive at the antenna phase center

Fig. 2 Denoised L1 double difference carrier-phase “true” residuals (i.e., carrier-phase multipath errors) of GPS PRN25 on DOYs 312 (top) and 313 (bottom) of 2022

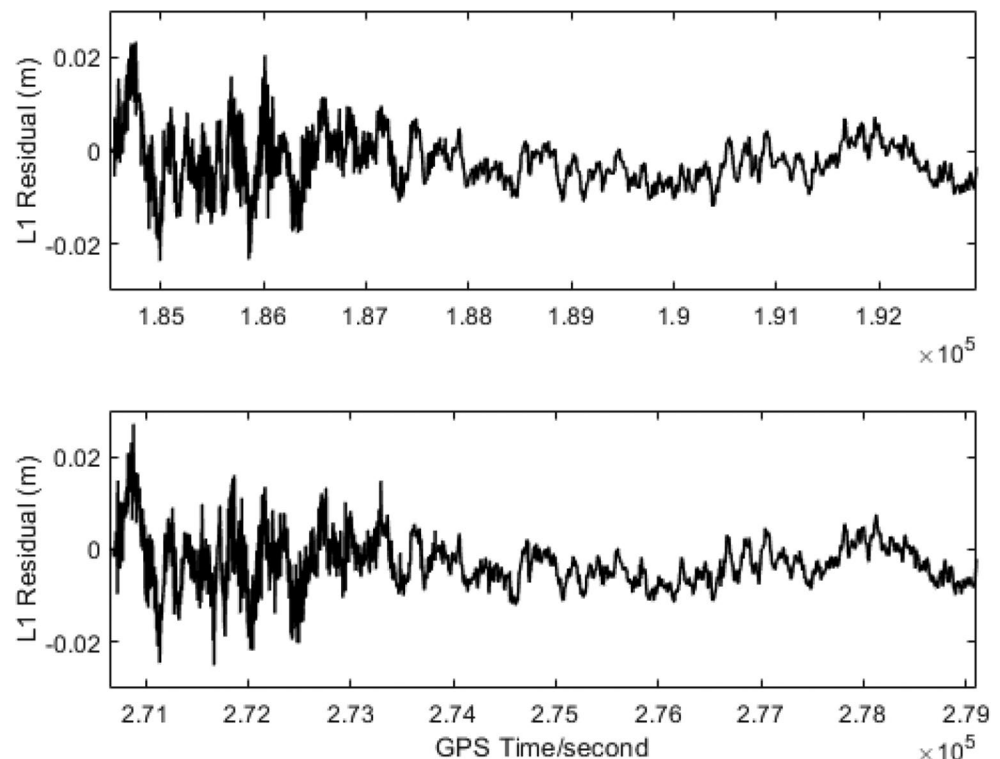


Fig. 3 Denoised L1 double difference carrier-phase “true” residuals (i.e., carrier-phase multipath errors) of GPS PRN25 on DOYs 312 (top), 313 (middle), 314 (bottom) of 2022. The rectangular window shows the difference in residuals between DOYs 314 and 312/313; there is no steel panel near the rover antenna on DOY 314, and there is a greater amplitude of residuals on DOYs 312 and 313. The complete statistical results of the Trimble R12 DOYs 312–314 data sets are described in Sect. 3.1 and Tables 4 and 5

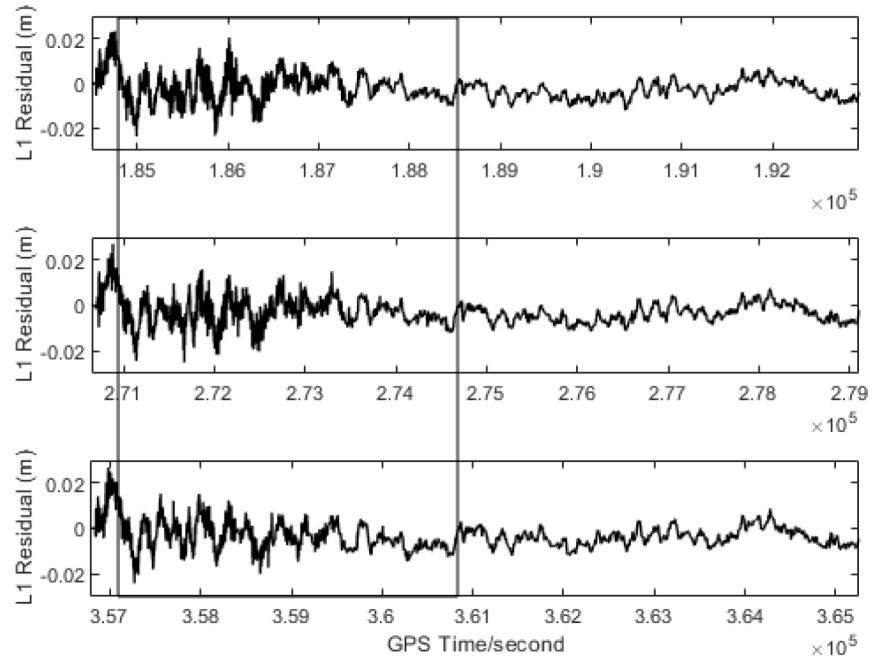


Table 4 Statistical results of all identified GNSS multipathing satellites collected with Trimble R12 with (i.e., DOYs 264, 312 and 313) and without (i.e., DOY314) the steel panel

	With steel panel		Without steel panel	
	RMS (mm)	Max. (mm)	RMS (mm)	Max (mm)
GPS				
L1	3.1	6.5	2.4	5.3
L5	3.2	9.4	2.9	9.3
Galileo				
E1	2.9	7.2	1.9	4.4
E5a	4.6	9.4	3.5	7.0
E5b	4.8	10.2	2.8	5.9
E5a+b	2.8	6.0	2.2	4.9
BDS				
B1	3.4	7.0	2.0	4.1
B2a	5.2	9.5	3.6	7.2
B3	5.0	9.5	4.0	9.4

from above and below the horizontal plane of the choking antenna.

Since the coordinates of the reference and rover stations are known, “true” DD carrier-phase residuals can be calculated as follows. For a given carrier-phase measurement:

$$\Phi_{L,ij}^{kl} = \rho_{L,ij}^{kl} - I_{L,ij}^{kl} + T_{ij}^{kl} + \lambda_L N_{L,ij}^{kl} + m_{L,ij}^{kl} + \epsilon_{L,ij}^{kl} \quad (1)$$

Table 5 RMS differences between the GPS L1 and L5 time series of the carrier-phase multipath errors with and without the steel panel

	GPS L1		GPS L5	
	DOY312–DOY313 (both days with the steel panel)	DOY313-DOY314 (DOY313 with the steel panel while DOY314 without the steel panel)	DOY312–DOY313 (both days with the steel panel)	DOY313-DOY314 (DOY313 with the steel panel while DOY314 without the steel panel)
RMS difference (mm)	0.23	1.18	0.17	0.62
Change (%)	-	408	-	261

where $\Phi_{L,ij}^{kl}$ denotes the DD phase observation (in meters) between satellites k and l , and stations i and j for the L carrier frequency, $\rho_{L,ij}^{kl}$ denotes the DD geometric range of the L carrier, $I_{L,ij}^{kl}$ denotes the DD ionospheric effect of the L carrier, T_{ij}^{kl} denotes the DD tropospheric delay, $N_{L,ij}^{kl}$ denotes the DD integer ambiguity of the L carrier, $m_{L,ij}^{kl}$ denotes the DD carrier-phase multipath error in the L carrier, $\epsilon_{L,ij}^{kl}$ denotes the DD measurement random error in the L carrier, and λ_L denotes the wavelength of the L carrier. The phase center variation (PCV) corrections for the antennas at satellites k and l and stations i and j are applied in the calculations for the geometric ranges of L carriers. The details of the PCV corrections can be found in Rothacher and Schmid (2010). The baseline for this investigation is only about 6 m. Therefore, the spatially correlated biases are eliminated. Equation (1) for very short baselines can be written as:

$$\Phi_{L,ij}^{kl} = \rho_{L,ij}^{kl} + \lambda_L N_{L,ij}^{kl} + m_{L,ij}^{kl} + \epsilon_{L,ij}^{kl} \quad (2)$$

As the coordinates of the reference and rover stations are known, the integer ambiguity can be determined. With the pre-determined integer ambiguity, Eq. (2) can be written as:

$$\Phi_{L,ij}^{kl} = \rho_{L,ij}^{kl} + m_{L,ij}^{kl} + \epsilon_{L,ij}^{kl} \quad (3)$$

Move the geometric range in Eq. (3) to the left-hand side, Eq. (3) becomes:

$$\Phi_{L,ij}^{kl} - \rho_{L,ij}^{kl} = m_{L,ij}^{kl} + \epsilon_{L,ij}^{kl} \quad (4)$$

The left-hand side of Eq. (4) is “the observed minus the computed” geometric range. The right-hand side of Eq. (4) is the “True” DD carrier-phase residuals because the computed geometric range is calculated from the known satellite and receiver coordinates (PCV corrected antenna phase centers), it contains only the DD carrier-phase multipath error and the carrier-phase measurement random error.

“True” DD carrier-phase residuals in the period determined in the previous step are extracted for Wavelet denoising (details about the Wavelet denoising process are described above). “True” DD carrier-phase residuals of a very short baseline (about 6 m) contain only DD carrier-phase multipath errors and DD carrier-phase measurement random errors (see the right-hand side of Eq. (4)). DD carrier-phase multipath errors are obtained after Wavelet denoising of the “true” DD carrier-phase residuals. More details can be found in Lau (2021).

Results and analysis

Effect of the steel panel on carrier-phase multipath errors

Figure 3 shows the L1 carrier-phase multipath errors of GPS satellite PRN 25 when using a Trimble R12 antenna at the rover station with the presence of the steel panel and without the steel panel. The statistical results of all identified GNSS multipathing satellites collected with Trimble R12 with (i.e., DOYs 264 (for BDS and Galileo), 312 and 313 (for GPS)) and without (i.e., DOY314) the steel panel are shown in Table 4. It is found that the RMS carrier-phase multipath errors of GNSS frequencies on DOYs 264, 312 and 313 are in the range of 2.8–5.2 mm, and the maximum multipath errors are in the range of 6.0–10.2 mm. After removing the steel panel on DOY 314, the RMS and maximum carrier-phase multipath errors are in the range of 1.9–4.0 mm and 4.1–9.4 mm, respectively. On average, the results show that the steel panel can generate 1–2 mm greater carrier-phase multipath errors than the ground/surrounding behind the steel panel. In terms of RMS and maximum errors of individual GNSS frequencies, carrier-phase multipath errors with the steel panel show a 1–4 mm increment when compared with no nearby steel panel. In terms of the percentage change of RMS errors in GNSS frequencies, carrier-phase

multipath errors with the steel panel increased in the range of 10–71% when compared to without the steel panel.

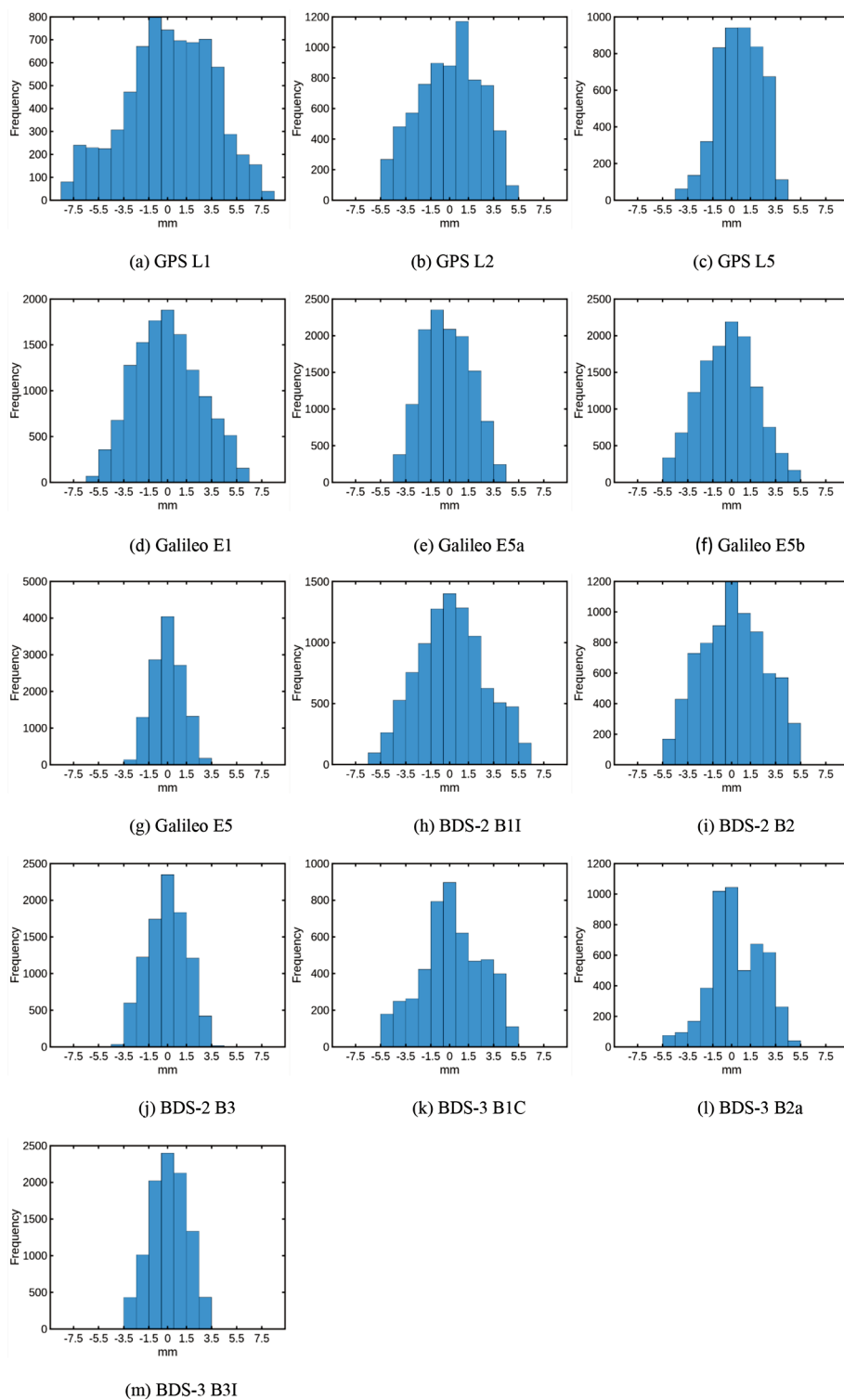
On the other hand, the effect of the steel panel on carrier-phase multipath errors can be shown by the differences between the time series of the carrier-phase multipath errors with and without the steel panel. Table 5 shows the RMS differences between the time series of the carrier-phase multipath errors with and without the steel panel. Columns 2 and 4 of Table 5 show the GPS L1 and L5 RMS differences between DOY312 and DOY313 (both days with the steel panel), respectively. Columns 3 and 5 of Table 5 show the GPS L1 and L5 RMS differences between DOY313 (with the steel panel) and DOY314 (without the steel panel), respectively. The results of the L1 and L5 RMS differences between DOY313 and DOY314 are about 3 to 4 times greater than those between DOY312 and DOY313. In other words, the carrier-phase multipath errors between DOY312 and DOY313 are very similar; the RMS differences are greatly less than 1 mm.

Choke-ring antenna mitigated carrier-phase multipath errors

Histograms of residual carrier-phase multipath errors of all identified GNSS multipathing satellites collected with Leica AR20 and Trimble GNSS-Ti-V2 antennas at the 95% confidence level are shown in Figs. 4 and 5, respectively. The results are summarized statistically in Table 6. The table shows the mean, SD, and maximum errors at the 95% confidence level per GNSS and frequency. The sample sizes of individual satellite signals/frequencies are in the range of 7657 to 23,086 epochs.

Comparing the statistical results between BDS-2 and BDS-3 satellites, the residual carrier-phase multipath errors of the two generations of satellites for both antennas are very similar (i.e., less than 0.5 mm differences in mean, SD and max., respectively, except for BDS-2 B1I and BDS-3 B1C but they have different spreading modulations). However, the residual carrier-phase multipath errors of B3 signals are less than B1 and B2 signals. It may suggest that the choke-ring antennas can mitigate multipath in the B3 signals better than the B1 and B2 signals. It may also indicate that the B3 signal design (i.e., BPSK(10); 1268.520 MHz) may have better multipath immunity than B1 and B2 signals. Similar findings can be seen for GPS L5 and Galileo E5 signals, which may suggest that the designs of the choke-ring antennas (e.g., the intervals of rings) are optimized better for mitigating multipath in the GPS L5 (wavelength: 25.5 cm), Galileo E5 (wavelength: 25.2 cm), BDS B3 (wavelength: 23.6 cm) frequency bands. On the other hand, BDS B1, Galileo E1, and GPS L1 show greater residual carrier-phase multipath errors, and the errors are in similar magnitudes.

Fig. 4 Histograms of residual carrier-phase multipath errors of all identified GNSS multipathing satellites collected with Leica AR20 antenna at the 95% confidence level. Note that not all GNSS satellites have the same number of frequencies such as some GPS satellites have no L5 signal

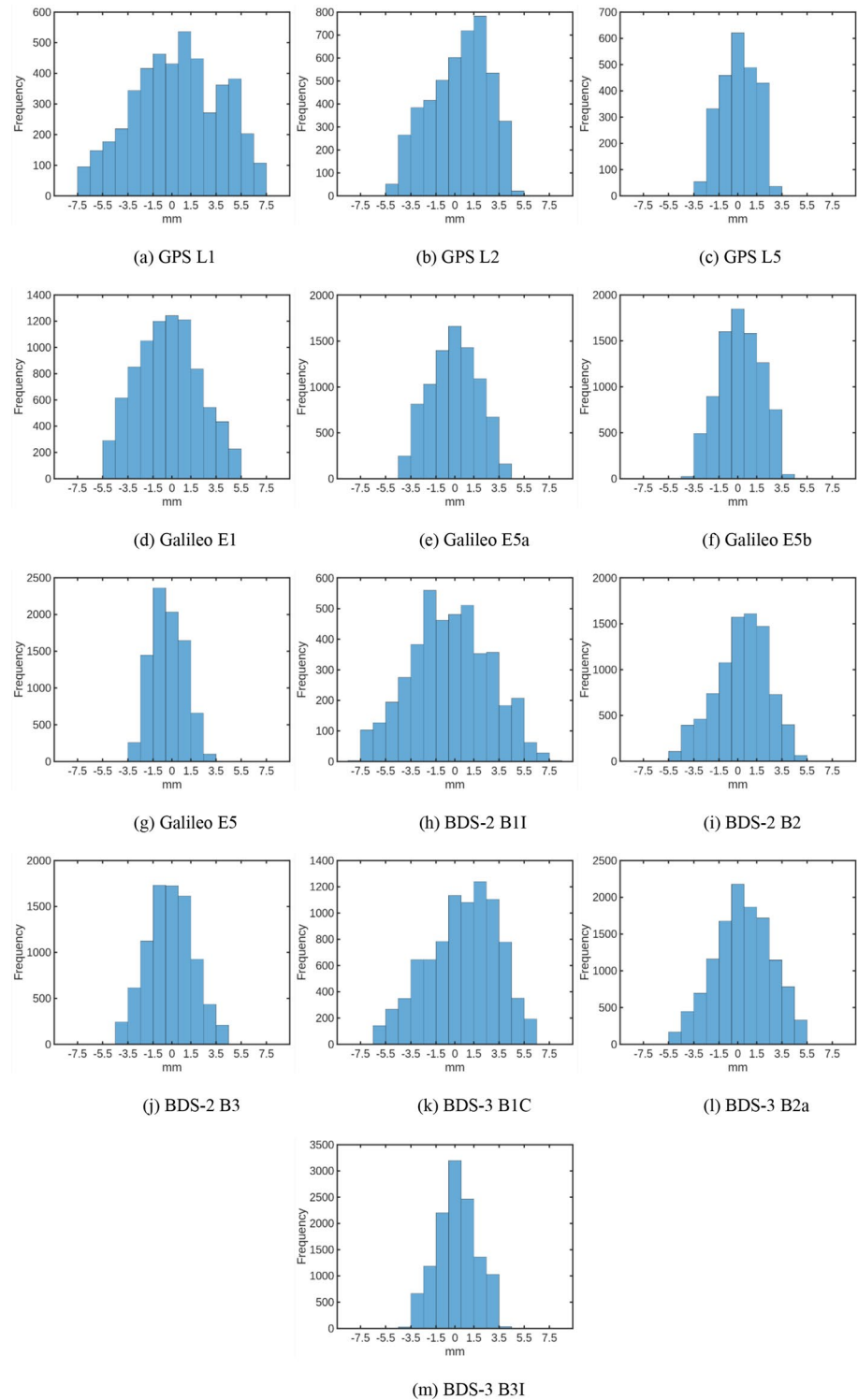


Spreading modulation design does affect code multipath effect (Hein et al. 2006). From the results in Table 6, residual carrier-phase multipath errors of GNSS signals with the Binary offset carrier (BOC) spreading modulation show similar magnitudes to those with the Binary Phase Shift Keying (BPSK) spreading modulation. It suggests that the

spreading modulation design may have insignificant or no impact on the carrier-phase multipath errors resulting from the Phase Lock Loop (PLL) tracking.

There is an assumption that the chance of multipath effect is high when the satellites are at low elevation angles. However, the magnitudes of carrier-phase multipath errors are

Fig. 5 Histograms of residual carrier-phase multipath errors of all identified GNSS multipathing satellites collected with Trimble GNSS-Ti-V2 antenna at the 95% confidence level. Note that not all GNSS satellites have the same number of frequencies (some GPS satellites have no L5 signal)



not directly proportional to the satellite elevation angles. Since the reflective surfaces in the vicinity of a GNSS antenna can face the antenna at different angles and surface-diffused GNSS signals can be reflected and arrive at the antenna, carrier-phase multipath errors have no strong correlation with satellite elevation angle. Therefore, the

work and findings of this article are not limited to certain and high/low-elevation angle satellites. Nevertheless, the statistical results obtained in this work cannot be used as the variance of carrier-phase multipath errors in stochastic models for a short period of observation time and RTK solutions because multipath errors are site-environment and

Table 6 Statistical results of all identified GNSS multipathing satellites collected. Blankets in the GNSS/frequency column show the RINEX 3.05 carrier-phase observation codes (Romero 2020) of the signals

GNSS/ frequency	Spreading modulation	Mean (mm)		SD (mm)		Max (mm)	
		AR20	GNSS-Ti-V2	AR20	GNSS-Ti-V2	AR20	GNSS-Ti-V2
BDS-2							
B1I (L2I)	BPSK(2)	2.1	2.6	1.6	1.8	6.0	7.5
B2 (L7I)	BPSK(2)	2.0	1.7	1.4	1.2	5.1	4.8
B3 (L6I)	BPSK(10)	1.3	1.5	0.9	1.0	3.6	4.2
BDS-3							
B1C (L1P)	QMBOC(6,1,4/33)	2.0	2.4	1.4	1.6	5.3	6.4
B2a (L5P)	BPSK(10)	1.6	1.8	1.2	1.3	4.9	5.3
B3I (L6I)	BPSK(10)	1.2	1.3	0.8	0.9	3.5	3.6
Galileo							
E1 (L1C)	CBOC(6,1,1/11)	2.1	2.0	1.5	1.4	5.8	5.5
E5a (L5Q)	AltBOC(15,10)	1.6	1.6	1.0	1.1	4.1	4.1
E5b (L7Q)	AltBOC(15,10)	1.8	1.4	1.3	0.9	5.3	3.6
E5 (L8Q)	AltBOC(15,10)	1.0	1.1	0.7	0.7	2.8	2.9
GPS							
L1 (L1C)	BPSK(1)	2.8	2.9	2.0	1.9	7.9	7.5
L2 (L2W)	BPSK(10)	2.1	2.0	1.3	1.2	5.1	4.7
L5 (L5Q)	BPSK(10)	1.5	1.2	1.0	0.7	3.8	2.8

Table 7 Statistical differences between Trimble GNSS-Ti-V2 and Leica AR20 antennas in GPS three frequencies. The data sets were collected on DOYs 265 and 267

Frequency	Δ Mean (mm)	Δ SD (mm)	Δ Max (mm)
L1	0.13	0.07	0.21
L2	0.08	0.10	0.37
L5	0.34	0.27	1.00

satellite-geometry dependent (see Fig. 3; the sign and magnitude of multipath errors of epochs are different even at the same site and with the same antennas). Moreover, the statistical results of carrier-phase multipath errors cannot be used as the error budget in integrity monitoring.

According to the statistics of the Leica AR20 and Trimble GNSS-Ti-V2 antennas in Figs. 4 and 5; Table 6, both antennas have very similar multipath mitigation performance. Note that the results shown in Figs. 4 and 5; Table 6 are obtained from multipathing satellites determined by side-real repeatability and ray-tracing as described in Sect. 2.3. Table 7 shows the differences in statistics (i.e., Δ mean, Δ SD and Δ max) at the 95% confidence level between Trimble GNSS-Ti-V2 (DOY 265) and Leica AR20 (DOY 267) antennas among GPS three frequencies. With these results of the repeated satellite orbits on different dates and different choke-ring antennas, no significant difference (not greater than 1 mm; negligible for cm/mm accuracy positioning) in the multipath mitigation performance between the Trimble and Leica antennas can be seen for all GPS frequencies.

Conclusion

GNSS is used widely in scientific and engineering applications. Some applications require centimeter or even millimeter positioning accuracy. Such applications must use high-precision carrier-phase measurements in relative observation mode (a reference station is needed). However, natural and man-made surfaces in the vicinity of GNSS antennas may cause reflected signals and result in centimeter/millimeter multipath errors in measurements (the magnitude of the error is similar to that of the required accuracy). Therefore, the multipath effect is the natural enemy of GNSS high-precision positioning.

GNSS signals are transmitted from GNSS satellites to GNSS receivers on the surface of the Earth. The first gateway for receiving the GNSS signal-in-space is the GNSS antenna. Choke-ring antennas are designed as the first gateway to mitigate the multipath effect in high-precision positioning. Any natural and man-made surfaces in the vicinity of the antenna may cause reflected GNSS signals. Choke-ring antennas cannot perfectly prevent reflected signals from arriving at the antenna phase centers. This work reveals the magnitudes of residual multipath effect on the high-precision carrier-phase measurements. It is found that the residual double-differencing carrier-phase multipath errors of GNSS frequencies can reach about 8 mm at the maximum, and the mean and SD are in a few millimeters at the 95% confidence level. Therefore, the multipath effect must be accounted for in high accuracy required deformation monitoring (e.g., for earthquakes) in order to prevent false alarms or wrong estimated deformation. Moreover, multipath mitigation is crucial for all real-time high accuracy required positioning

applications because multipath errors affect positioning accuracy and correctness/success of ambiguity resolution.

It must be emphasized that the determined carrier-phase multipath errors cannot be used as a statistical parameter, such as standard error for stochastic models and error budget computation, because multipath errors are time and site environment dependent (see Fig. 3; the sign and magnitude of multipath errors of epochs are different even at the same site and with the same antennas). Moreover, this work has found no significant difference in multipath mitigation performance between Trimble GNSS-Ti-V2 and Leica AR20 antennas for all GPS frequencies (see Sect. 3.2 and Table 7).

Acknowledgements This research was funded by the Hong Kong Polytechnic University, grant number 1-BD6G. The author thanks A. Mack for his help in fieldwork and data pre-processing.

Author contributions All the work in this article was performed by the author.

Funding Open access funding provided by The Hong Kong Polytechnic University
This research was funded by the Hong Kong Polytechnic University, grant number 1-BD6G.

Data availability Data sets generated during the current study are available from the corresponding author on reasonable request.

Declarations

Consent for publication Not applicable.

Competing interests The authors declare no competing interests.

Conflict of interest The authors declare no competing interests.

Ethical approval and consent to participate Not applicable.

Open Access This article is licensed under a Creative Commons Attribution 4.0 International License, which permits use, sharing, adaptation, distribution and reproduction in any medium or format, as long as you give appropriate credit to the original author(s) and the source, provide a link to the Creative Commons licence, and indicate if changes were made. The images or other third party material in this article are included in the article's Creative Commons licence, unless indicated otherwise in a credit line to the material. If material is not included in the article's Creative Commons licence and your intended use is not permitted by statutory regulation or exceeds the permitted use, you will need to obtain permission directly from the copyright holder. To view a copy of this licence, visit <http://creativecommons.org/licenses/by/4.0/>.

References

- Agnew DC, Larson KM (2007) Finding the repeat time of the GPS Constellation. *GPS Solutions* 11(1):71–76
- Blewitt G, Heflin MB, Hurst KJ, Jefferson DC, Webb FH, Zumberge JF (1993) Absolute far-field displacements from the 28 June 1992 Landers earthquake sequence. *Nature* 361:340–342. <https://doi.org/10.1038/361340a0>
- ComNav (2024) ComNav Technology CORS Solution https://http://v1.cecdn.yun300.cn/fsite_1802020370/ComNav_CORS_Solution_2.01561382800309.pdf. Accessed 8 March 2024
- Farquharon JI, Amelung F (2020) Extreme rainfall triggered the 2018 rift eruption at Kīlauea Volcano. *Nature* 580:491–495. <https://doi.org/10.1038/s41586-020-2172-5>
- Fenton P, Jones J (2005) The Theory and Performance of NovAtel Inc.'s Vision Correlator. Proceedings of the 18th International Technical Meeting of the Satellite Division of The Institute of Navigation (ION GNSS 2005), Long Beach, CA, September 2005, pp. 2178–2186
- Filippov V, Tatarnicov D, Ashjaee J, Astakhov A, Sutiagin I (1998) The First Dual-Depth Dual-Frequency Choke Ring. Proceedings of the 11th International Technical Meeting of the Satellite Division of The Institute of Navigation (ION GPS 1998), Nashville, TN, September 1998, pp. 1035–1040
- Hager BH, Dieterich J, Frohlich C, Juanes R, Mantica S, Shaw JH, Bottazzi F, Caresani F, Castineira D, Cominelli A, Meda M, Osculati L, Petroselli S, Plesch A (2021) A process-based approach to understanding and managing triggered seismicity. *Nature* 595:684–689. <https://doi.org/10.1038/s41586-021-03668-z>
- Hein GW, Avila-Rodriguez J-A, Wallner S, Pratt AR, Owen J, Issler J, Betz JW, Hegarty CJ, Lenahan S, Rushanan JJ, Kraay AL, Stansell TA (2006) MBOC: The New Optimized Spreading Modulation Recommended for GALILEO L1 OS and GPS L1C. Proceedings of the 2006 IEEE/ION Position, Location, And Navigation Symposium, Coronado, CA, USA, 2006, pp. 883–892
- IGS (2015) IGS Site Guidelines. Infrastructure Committee, Central Bureau. <https://files.igs.org/pub/station/general/IGS%20Site%20Guidelines%20July%202015.pdf>. Accessed on 8 March 2024
- Lau L (2012) Comparison of measurement and position domain multipath filtering techniques with the repeatable GPS orbits for static antennas. *Surv Rev* 44:9–16
- Lau L (2017) Wavelet packets based Denoising Method for Measurement Domain repeat-time Multipath Filtering in GPS Static High-Precision Positioning. *GPS Solutions* 21(2):461–474
- Lau L (2021) GNSS multipath errors and mitigation techniques. In: Petropoulos GP, Srivastava PK (eds) *GPS and GNSS Technology in Geosciences*. Elsevier, pp 77–98
- Lau L, Cross P (2007) Development and testing of a New Ray-tracing Approach to GNSS Carrier-Phase Multipath Modelling. *J Geodesy* 81(11):713–732
- Pieuch CG, Huybers P, Hay CC, Kemp AC, Little CM, Mitrovica JX, Ponte RM, Tingley MP (2018) Origin of spatial variation in US East Coast sea-level trends during 1900–2017. *Nature* 564:400–404. <https://doi.org/10.1038/s41586-018-0787-6>
- Roman A, Lundgren P (2021) Dynamics of large effusive eruptions driven by caldera collapse. *Nature* 592:392–396. <https://doi.org/10.1038/s41586-021-03414-5>
- Romero I (2020) RINEX the Receiver Independent Exchange Format Version 3.05. IGS/RTCM RINEX WG Chair ESA/ESOC/Navigation Support Office, Darmstadt, Germany
- Rothacher M, Schmid R (2010) ANTEX: The Antenna Exchange Format, Version 1.4. <https://files.igs.org/pub/data/format/antex14.txt>. Accessed 18 July 2024
- Schupler BR, Clark TA (2001) Characterizing the Behavior of Geodetic GPS Antennas. *GPS World*, February 2001: 48–55
- Seeber G, Menge F, Völksen C, Wübbena G, Schmitz M (1998) Precise GPS Positioning Improvements by Reducing Antenna and Site Dependent Effects. International Association of Geodesy Symposia, 118, 3–9 September 1997, Rio de Janeiro, Brazil, Springer Verlag
- Smittarello D, Smets B, Barrière J, Michellier C, Oth A, Shreve T, Grandin R, Theys N, Brenot H, Cayol V, Allard P, Caudron C,

- Chevrel O, Darchambeau F, de Buyl P, Delhaye L, Derauw D, Ganci G, Geirsson H, Kamate Kaleghetso E, Kambale Makundi J, Kambale Nguomoja I, Kasereka Mahinda C, Kervyn M, Kimanuka Ruriho C, Le Mével H, Molendijk S, Namur O, Poppe S, Schmid M, Subira J, Wauthier C, Yalire M, d'Oreye N, Kervyn F, Syavulisembo Muhindo A (2022) Precursor-free eruption triggered by edifice rupture at Nyiragongo volcano. *Nature* 609:83–88. <https://doi.org/10.1038/s41586-022-05047-8>
- Tang S, Liu H, He S (2013) Analysis of Multipath Effect on the Antennas of CORS Receivers. In: Sun, J., Jiao, W., Wu, H., Shi, C. (eds) China Satellite Navigation Conference (CSNC) 2013 Proceedings. Lecture Notes in Electrical Engineering, vol 244. Springer, Berlin, Heidelberg. https://doi.org/10.1007/978-3-642-37404-3_30
- Tatarnikov D, Astakhov A, Stepanenko A (2011) Broadband convex impedance ground planes for multi-system GNSS reference station antennas. *GPS Solut* 15:101–108. <https://doi.org/10.1007/s10291-010-0172-x>

Publisher's note Springer Nature remains neutral with regard to jurisdictional claims in published maps and institutional affiliations.